Counting electrons - a new approach to tailor the hydrogen sorption properties of high-entropy alloys

Magnus Moe Nygård[a,*], Gustav Ek[b], Dennis Karlsson[b], Magnus H. Sørby[a], Martin Sahlberg[b], Bjørn C. Hauback[a]

[a] *Institute for Energy Technology, Department of Neutron Materials Characterization, P.O. Box 40, NO-2027 Kjeller, Norway*
[b] *Department of Chemistry - Ångström Laboratory, Uppsala University, Box 523, SE-75120 Uppsala, Sweden*

Abstract

We have investigated the structure and hydrogen storage properties of a series of quaternary and quintary high-entropy alloys related to the ternary system TiVNb with powder X-ray diffraction (PXD), scanning electron microscopy (SEM), thermogravimetric analysis (TGA), differential scanning calorimetry (DSC) and manometric measurements in a Sieverts apparatus. The alloys have body-centred cubic (bcc) crystal structures and form face-centred cubic (fcc) metal hydrides with hydrogen-to-metal ratios close to 2 by hydrogenation. The onset temperature for hydrogen desorption, T_{onset}, decreases linearly with the valence-electron concentration, *VEC*. Moreover, the volumetric expansion per metal atom from the bcc alloys to the fcc hydrides, $[(V/Z)_{\mathrm{fcc}} - (V/Z)_{\mathrm{bcc}}]/(V/Z)_{\mathrm{bcc}}$, increases linearly with the *VEC*. Therefore, it seems that a larger expansion of the lattice destabilizes the metal hydrides and that this effect can be tuned by altering the *VEC*. Kissinger analyses performed on the DSC measurements indicate that the destabilization is a

*Corresponding author: magnus.moe.nygaard@ife.no

thermodynamic rather than kinetic effect.

Based upon these insights we have identified $TiVCrNbH_8$ as a material with suitable thermodynamics for hydrogen storage in the solid state. This HEA-based hydride has a reversible hydrogen storage capacity of 1.96 wt.% H at room temperature and moderate H_2-pressures. Moreover, it is not dependent on any elaborate activation procedure to absorb hydrogen.

Keywords: metal hydrides, hydrogen storage, high-entropy alloys, HEAs

1. Introduction

The international community is currently experiencing a big increase in the harvest of renewable energy, for instance through windturbines and photovoltaics [1]. However, the energy output from these technologies is heavily reliant on shifting conditions, such as wind-speed, cloudiness and other weather related phenomena. Moreover, they can rarely provide immediate response to the commercial demand of energy. Thus, it is necessary to implement large-scale energy storage systems into the electrical power grid. In this context, hydrogen is considered as one of the most attractive energy carriers due to its simple and efficient conversion, as well as its superior gravimetric energy density when compared to any known fuel. The technology is especially attractive if the hydrogen storage unit is coupled to a Proton Exchange Membrane Fuel Cell (PEMFC) as it is not limited by the Carnot efficiency [2]. Hence, electrical efficiencies above 50% is achievable at temperatures below 100 °C. Still, the low density of hydrogen stored at 700 bar remains a challenge for efficient storage. One promising solution is to store the hydrogen in the solid-state using metal hydrides. This solution is in general

attractive as metal hydrides can be made to operate at low pressures and non-cryogenic temperatures while achieving very high volumetric hydrogen densities. A wide variety of different metal hydrides has been suggested for this purpose, i.e. intermetallic hydrides and complex hydrides [3]. Complex hydrides can achieve the highest gravimetric hydrogen densities among metal hydrides, such as 18.4 wt.% H in $LiBH_4$ [4]. Unfortunately, their kinetics and thermodynamics usually prevent applications at ambient temperatures and they are often subject to non-reversibility during hydrogen sorption [5–9]. In the case of intermetallic hydrides formed from alloys of type AB, AB_2, AB_5, etc., common drawbacks include degradation after repeated hydrogen absorption/desorption cycling, surface passivation and slow hydrogen sorption kinetics [10–13]. Moreover, the alloys often contain expensive elements and the reversible gravimetric hydrogen density is usually lower than 2 wt.% H [14]. On the other hand, these materials achieve among the highest volumetric hydrogen densities, i.e. 150 g H/L in Mg_2FeH_6 [15] making them attractive for stationary, maritime and heavy duty utility vehicle applications [3]. The hydrogen storage properties can in many cases be enhanced by carefully tuning the elemental composition of either A, B or both [16–18]. However, the tunability is restricted by the degree of solubility that can be achieved in the alloy. The Hume–Rothery rules states that the solute and solvent atoms should have comparable atomic radii, electronegativity and valency to enable a complete solvation. As can be seen from table 1, these parameters vary significantly between the transition metals and therefore only small amounts of one element can usually be dissolved in another or vice versa.

Recently a novel alloying strategy has emerged in which four or more

Table 1: Atomic numbers Z, atomic radii r, valence-electron concentrations VEC and electronegativities by Pauling scale χ_P for a selection of elements [19].

Element	Z [∅]	r [Å]	VEC [∅]	χ_P [∅]
Ti	22	1.46	4	1.54
V	23	1.32	5	1.63
Cr	24	1.25	6	1.66
Mn	25	1.35	7	1.55
Fe	26	1.24	8	1.83
Co	27	1.25	9	1.88
Ni	28	1.25	10	1.91
Cu	29	1.28	11	1.90
Zn	30	1.39	12	1.65
Zr	40	1.60	4	1.33
Nb	41	1.43	5	1.60
Mo	42	1.36	6	2.16
Ru	44	1.34	8	2.20
Rh	45	1.35	9	2.28
Hf	72	1.58	4	1.30
Ta	73	1.43	5	1.50

principle elements are mixed in an equimolar (or near-equimolar) compositions. Such alloys, that are referred to as high-entropy alloys (HEAs), tend to form single-phase solid solutions with simple structures such as body-centred cubic (bcc) or cubic close-packed (ccp) [19]. Hence, the different elements are randomly distributed over a single crystallographic site and the alloys are

characterized by being heavily disordered. Which structure that is formed can often be predicted *a priori* from the valence-electron concentration, *VEC*, of the HEA which is defined as

$$VEC = \sum_{i=1}^{N} \{c_i (VEC)_i\} \tag{1}$$

where c_i is the atomic fraction of element i with valence-electron concentration $(VEC)_i$ present in the alloy. According to Guo et al. [20] and Poletti and Battezzati [21], a ccp phase is obtained if $VEC > 7.6$, whereas a bcc phase is obtained if $VEC < 7.6$. It appears that a larger degree of solubility can be achieved in HEAs than what is suggested by the Hume–Rothery rules. This enables a larger degree of property-tuneability. Hydrogen storage has been suggested as an application area for HEAs [19], but the field is in its infancy with only a few reported studies [22–34]. These works demonstrate that the hydrogen storage properties of HEAs can be dramatically different than in the binary hydrides based on the isolated elements. For instance, TiVZrNbHf was reported to absorb hydrogen so that [H]/[M] ~ 2.5 [25]. This is 25% higher than what has been reported for the corresponding binary hydrides such as TiH_2 and ZrH_2. Unfortunately, the investigated HEA-based hydrides are too stable for applications at ambient conditions [28–30, 32]. Before such applications can be considered it is therefore necessary to develop a strategy to destabilize HEA-based hydrides.

In this work, we report a systematic investigation of the hydrogen storage properties for a series of quaternary and quintary HEAs related to the ternary system TiVNb. The investigated systems includes TiVNb, TiVCrMo, TiZrNbHf, TiVZrNbHf, TiVCrNbMo, TiVCrNbTa and TiVNbM with $M \in$

{Cr, Zr, Mo, Hf, Ta}. These systems have *VEC* ranging from 4.25 (TiZrNbHf) to 5.25 (TiVCrMo). We show how the stability of HEA-based metal hydrides can be estimated *a priori* from the *VEC*. We also provide a structural explanation to the destabilization mechanism and show that it is a thermodynamic effect rather than a kinetic one. Based upon these findings, we demonstrate reversible hydrogen storage at room temperature (*RT*) in a TiVCrNb HEA that is not dependent on any activation procedure.

2. Experimental

2.1. Synthesis.

TiVNb, seven quaternary HEAs of TiVCrMo, TiZrNbHf and TiVNbM with $M \in \{\mathrm{Cr, Zr, Mo, Hf, Ta}\}$, and three quintary HEAs of TiVZrNbHf, TiVCrNbMo and TiVCrNbTa are investigated in this work. Alloys with the compositions TiVNbM with $M \in$ {Mn, Fe, Ni, Cu, Ru, Rh}, were also synthesized, but did not assume single-phase bcc structures in the as cast state. Thus, they are not discussed in further detail. All the alloys were synthesized from lumps of Ti, Cr, Cu, Nb, Ru, Rh, Ta (Goodfellow, 99.99% metals basis), V (Goodfellow, 99.6% metals basis), Mn (Goodfellow, 99.98% metals basis), Fe (Goodfellow, 99.95% metals basis), Ni (Goodfellow, 99% metals basis), Zr (Alfa Aesar, 95.8% metals basis), Mo (Goodfellow, 99.9% metals basis) and Hf (Goodfellow, 97% metals basis) by arc melting under Ar atmosphere. Ti oxygen-getter pieces were melted initially and the samples were subsequently turned and remelted five times to enhance their homogeneity. The final compositions are very close to the nominal ones as the mass losses during arc-melting were less than 1 wt.%. TiVCrNbMo and the M = Cr, Mo

samples were very brittle and could easily be crushed to a fine powder using a hammer. The other alloys were on the contrary extremely hard and were filed into coarse powders with an iron file for phase identification with powder X-ray diffraction. The rest were cut into smaller pieces with a long handled bolt cutter. These pieces were subsequently loaded into an in-house built Sieverts apparatus [35] where they were heated to 355 ± 5 °C under dynamic vacuum for 1-2 hours for activation. The only exception was TiZrNbHf which was heated to 522 °C. The samples were then cooled to *RT* and exposed to gaseous hydrogen at 23.6 ± 1.8 bar in a single pulse. The samples were left under these conditions until the change in pressure was below the measurement uncertainty of the pressure transducer ($\pm$ 0.3 bar). The final pressure was typically at 14.5 ± 1.3 bar. For some of the samples (TiZrNbHf, TiVZrNbHf, TiVNbMo, TiVCrNbTa, TiVCrNbMo and TiVCrMo) the pressure was then raised to 95 ± 5 bar. However, this did not result in any significant further hydrogen uptake. TiVCrNb was also hydrogenated with no activation procedure. In that case, as cast TiVCrNb was stored in air for 5 days before it was loaded into the Sieverts apparatus and directly exposed to gaseous hydrogen. After an incubation time of 360 min the sample absorbed hydrogen and a full hydride was achieved within a few minutes. The pressure was stable within the measurement uncertainty at 20.2 bar H_2 after the absorption was complete. All sample handling and storage was otherwise performed inside an MBraun Unilab glovebox with purified Ar atmosphere (< 1 ppm O_2 and H_2).

2.2. Powder X-ray diffraction (PXD).

Laboratory PXD patterns were measured for TiZrNbHf, $TiZrNbHfH_x$, $TiVNbMoH_x$, $TiVCrNbTaH_x$, TiVCrMo, $TiVCrMoH_x$, TiVCrNbMo and $TiVCrNbMoH_x$ with a Bruker D8 Advance diffractometer with Cu-Kα radiation ($\lambda_{K\alpha1} = 1.5406$ Å, $\lambda_{K\alpha2} = 1.5444$ Å). For the other investigated HEAs and their corresponding hydrides, synchrotron radiation (SR) PXD patterns were measured at the Swiss-Norwegian beamlines (SNBL) BM01 and BM31 at the European Synchrotron Radiation Facility (ESRF) in Grenoble, France using a Dectris Pilatus 2M detector [36] with a fixed X-ray wavelength of $\lambda = 0.6866$ Å and a CMOS DEXELA 2D detector with a fixed X-ray wavelength of $\lambda = 0.3171$ Å, respectively. During these measurements, the alloys and hydrides were contained in 0.8 mm and 0.5 mm borosilicate glass capillaries, respectively. These were all filled and sealed under Ar. The M = Cr sample was also measured in a 0.8 mm inner-diameter sapphire capillary under 45 bar H_2. Phase identification was performed by search-matches with the PDF-4 database. Further analysis was performed with the Rietveld method using the General Structure Analysis System II (GSAS-II) [37]. In a typical refinement the background was fitted by a 16^{th} order shifted Chebyschev polynomial. The peaks were modelled by a Thompson-Cox-Hastings pseudo-Voigt function [38] with 4 refineable parameters. The displacement parameters were also refined.

2.3. Scanning electron microscopy (SEM).

The elemental composition was studied by energy dispersive X-ray spectroscopy (EDS) in a Zeiss Merlin SEM equipped with an Ultim Max 100 mm^2 silicon drift detector. The data was acquired using an acceleration voltage of 20 kV and a beam current of 1 nA for 20 min at a working distance of

8.5 mm. The data was evaluated using the AZtec software. Prior to analysis the samples were prepared by mechanical grinding using 220 grit SiC paper, followed by polishing using 9 μm, 3μm and 1μm diamond suspensions. Finally, the samples were polished using a H_2O_2:SiO_2 (1:5 ratio) mixture.

2.4. Thermal analysis.

Thermogravimetric analysis (TGA) and differential scanning calorimetry (DSC) were measured simultaneously with a heat flux type Netzsch STA 449 F3 Jupiter apparatus. In a typical measurement a ~ 45 mg sample was placed inside an alumina crucible equipped with a pierced lid. The measurement was conducted under flowing Ar at 50 mL/min. The samples were briefly exposed to air when they were loaded into the apparatus. The gravimetric measurements of the hydrogen contents were taken as the mean value of several measurements and the corresponding standard deviations were taken as the uncertainty. Furthermore, the measurements were conducted at four different heating rates, 2, 5, 10 and 20 °C/min, for Kissinger analyses.

2.5. Sieverts measurements.

Kinetics of hydrogen absorption were measured manometrically with an in-house built Sieverts apparatus [35].

3. Results and discussion

The HEAs investigated in this work are summerized in table 2. All the alloys assume single-phase bcc ($Im\overline{3}m$) structures in the as cast state. The microstructure of TiVNb, TiVZrNbHf, TiVCrMo, TiVCrNbMo and TiVNbM with $M \in \{\mathrm{Cr}, \mathrm{Zr}, \mathrm{Ta}\}$ were investigated using SEM and EDS. Fig. 1 shows

backscattered electron images and EDS mappings for TiVNb, TiVCrNb and TiVCrMo. The EDS results are summarized in table 3. Corresponding measurements for TiVCrNbMo can be found in fig. A.1 and table A.1 in the supplementary information, while measurements for TiVZrNb, TiVNbTa and TiVZrNbHf have been reported elsewhere [27, 34]. The alloys have dendritic microstructures with different chemical compositions in the dendritic and interdendritic areas. Nevertheless, the variation in *VEC* deviates less than 4 % from that of the nominal compositions, and usually by less than 1 %. Therefore, the nominal value for the *VEC* can be considered as representative for the overall alloys.

The alloys were activated by heating to 355 ± 5 °C under dynamic vacuum for 1-2 hours to enable hydrogen sorption to commence at reasonable timescales. However, TiVCrNb was not dependent on such activation procedures even after storage in air for 5 days. The resultant hydrides are single-phase face-centred cubic (fcc, $Fm\overline{3}m$) if $VEC < 4.75$. When $VEC \geq 4.75$, the hydrides assume a fcc/bcc multiphase composition when retrieved from the Sieverts apparatus. The amount of fcc in the multiphase decreases with *VEC* and eventually reaches zero for TiVCrNbMo ($VEC = 5.20$). $TiZrNbHfH_8$ is the only hydride that deviates from the general trend. In this case, the hydride assumes a pseudo-fcc structure with a slight body-centred tetragonal deformation (bct, $I4/mmm$). The lattice parameters are $a_{\mathrm{bct}} = 3.3007(6)$ Å and $c_{\mathrm{bct}} = 4.5959(8)$ Å. The corresponding volume per metal atom is $(V/Z)_{\mathrm{bct}} = 25.04(2)$. A similar bct structure has been observed for $TiVZrNbHfH_{12.5}$ [25, 27], but in this work $TiVZrNbHfH_{10}$ is obtained as a single-phase fcc. We have not been able to reproduce the

Table 2: Comparison of the valence-electron concentration *VEC*, lattice parameters *a.*, volume per atom (V/Z). and lattice expansion α for the considered bcc HEAs and their corresponding fcc hydrides.

Sample	M	VEC [∅]	a_{bcc} [Å]	$(V/Z)_{\mathrm{bcc}}$ [Å^3]	a_{fcc} [Å]	$(V/Z)_{\mathrm{fcc}}$ [Å^3]	α [∅]
TiZrNbHf	n/a	4.25	3.4290(6)	20.16(2)	n/a	n/a	0.242(2)
TiVZrNbHf	ZrHf	4.40	3.3573(7)	18.92(2)	4.5784(1)	23.993(8)	0.268(1)
TiVZrNb	Zr	4.50	3.3029(3)	18.02(1)	4.5291(2)	23.22(1)	0.2886(9
TiVNbHf	Hf	4.50	3.2975(4)	17.92(1)	4.5174(1)	23.047(7)	0.2861(8
TiVNb	∅	4.67	3.2000(2)	16.382(5)	4.4296(1)	21.728(7)	0.3263(6
TiVNbTa	Ta	4.75	3.2277(2)	16.813(5)	4.4355(4)	21.815(5)	0.2975(5
TiVCrNb	Cr	5.00	3.1243(1)	15.249(3)	4.3963(3)	21.24(2)	0.393(1)
TiVNbMo	Mo	5.00	3.1806(1)	16.088(4)	n/a	n/a	n/a
TiVCrNbTa	CrTa	5.00	3.1816(2)	16.103(6)	n/a	n/a	n/a
TiVCrNbMo	CrMo	5.20	3.135(2)	15.41(5)	n/a	n/a	n/a
TiVCrMo	n/a	5.25	3.0736(5)	14.52(1)	n/a	n/a	n/a

high [H]/[M] reported earlier for TiVZrNbHf.

Fig. 2 shows Rietveld refinements for the SR-PXD patterns of the different states of the TiVCrNb HEA ($VEC = 5.0$). Note from this figure that a single-phase fcc hydride is obtained for this composition when it is placed under 45 bar H_2. The bcc phase of TiVCrNb is retrieved when the $TiVCrNbH_x$ is heated to 600 °C. If the hydride is heated to 1000 °C it decomposes into a multiphase composition that consists of a bcc phase ($a_{\mathrm{bcc}} = 3.24862(8)$ Å), a C15 Laves phase ($a_{\mathrm{C15}} = 7.1623(1)$ Å) and a small fraction of an unidentified compound. Corresponding Rietveld refinements for the other alloys and

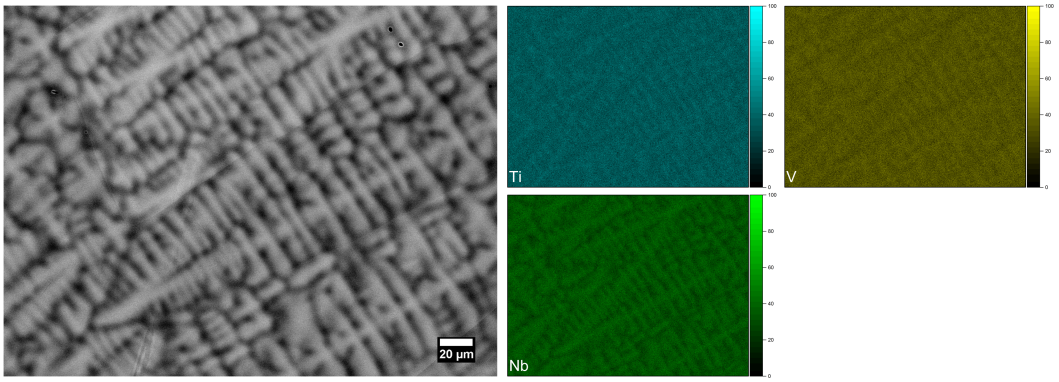

(a) TiVNb

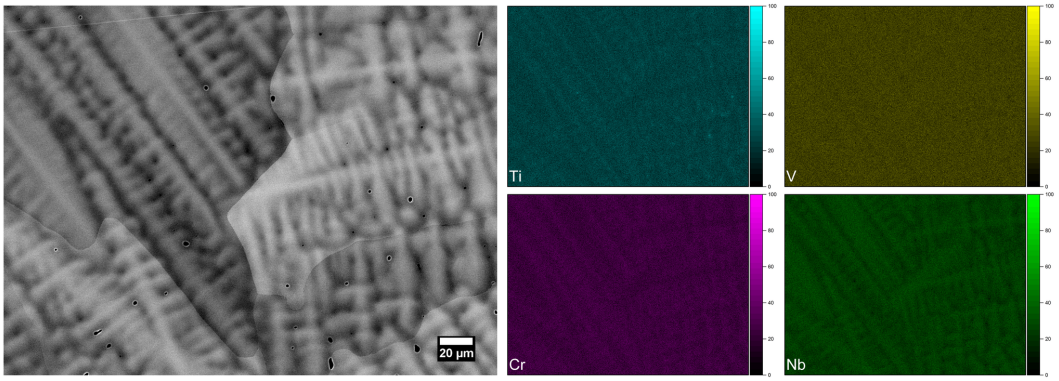

(b) TiVCrNb

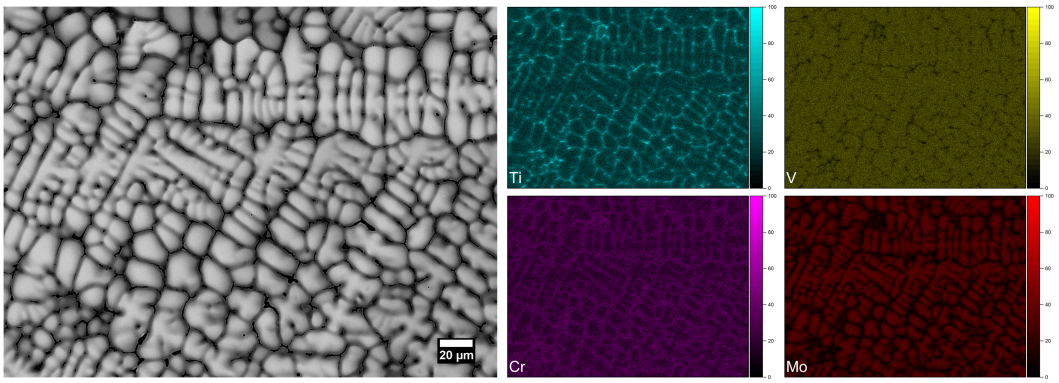

(c) TiVCrMo

Fig. 1: Backscattered electron images (left) and EDS maps (right) of as cast TiVNb **(a)**, TiVCrNb **(b)** and TiVCrMo **(c)**.

Table 3: The composition of TiVNb, TiVCrNb and TiVCrMo measured by EDS. VEC values for different compositions are shown for comparison.

	Composition					
System	Ti	V	Cr	Nb	Mo	VEC [∅]
TiVNb (nominal)	0.33	0.33	-	0.33	-	4.67
TiVNb (average)	0.35	0.33	-	0.32	-	4.65
TiVNb (dendrite)	0.34	0.32	-	0.35	-	4.71
TiVNb (interdendrite)	0.36	0.35	-	0.29	-	4.64
TiVCrNb (nominal)	0.25	0.25	0.25	0.25	-	5.00
TiVCrNb (average)	0.26	0.25	0.25	0.24	-	4.99
TiVCrNb (dendrite)	0.25	0.25	0.24	0.26	-	4.99
TiVCrNb (interdendrite)	0.26	0.25	0.26	0.23	-	5.00
TiVCrMo (nominal)	0.25	0.25	0.25	-	0.25	5.25
TiVCrMo (average)	0.28	0.25	0.24	-	0.22	5.13
TiVCrMo (dendrite)	0.23	0.27	0.22	-	0.28	5.27
TiVCrMo (interdendrite)	0.37	0.23	0.28	-	0.12	5.03

hydrides are presented in fig. A.2 and A.3 in the supplementary information. The lattice parameters, a_{bcc} and a_{fcc}, as well as the volumes per metal atom, $(V/Z)_{\mathrm{bcc}}$ and $(V/Z)_{\mathrm{fcc}}$, of the bcc HEAs and their corresponding single-phase fcc hydrides are shown in table 2.

We define α, the expansion of the volume per metal atom from the bcc HEA to the corresponding hydride, as

$$\alpha = [(V/Z)_{\mathrm{fcc}} - (V/Z)_{\mathrm{bcc}}]/(V/Z)_{\mathrm{bcc}} \tag{2}$$

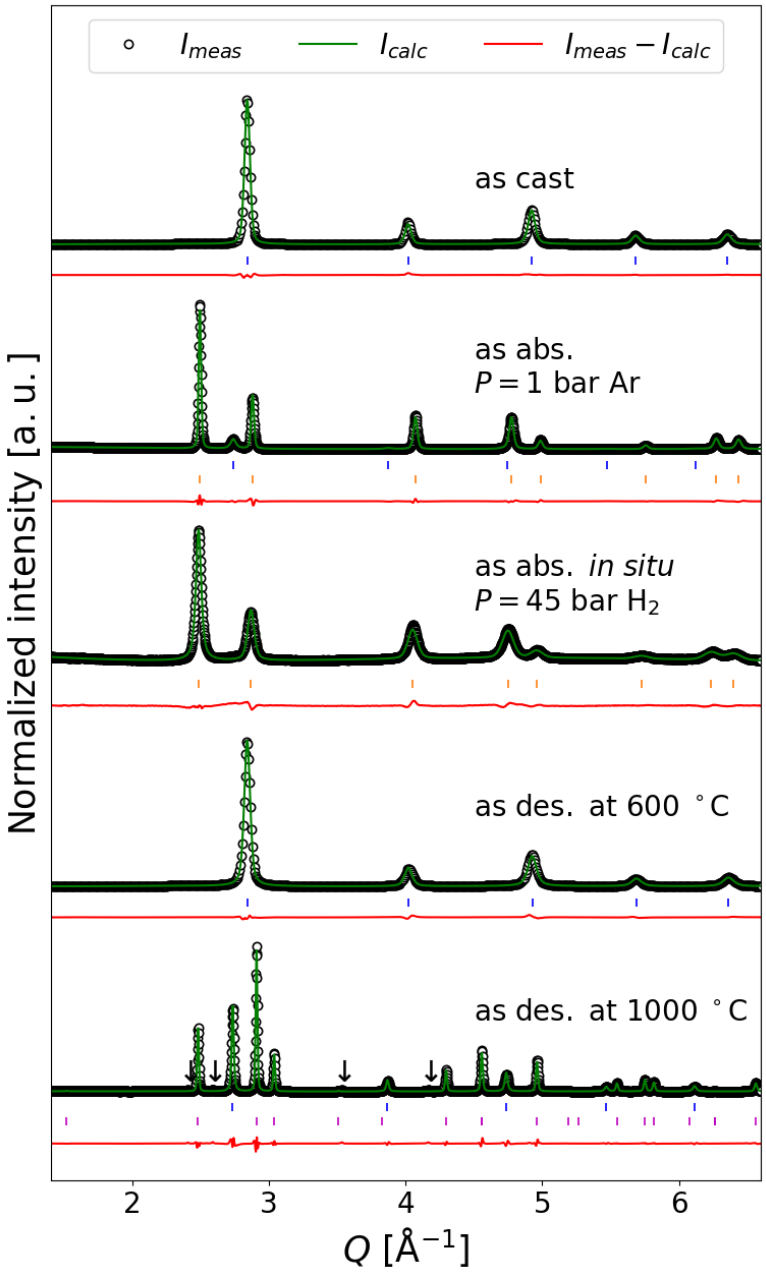

Fig. 2: Rietveld refinements to the SR-PXD patterns of TiVCrNb in its different states. | indicates a bcc phase ($Im\bar{3}m$), | indicates a fcc phase ($Fm\bar{3}m$) and | indicates a C15 Laves phase ($Fd\bar{3}m$). Peaks belonging to an unidentified compound are marked with arrows.

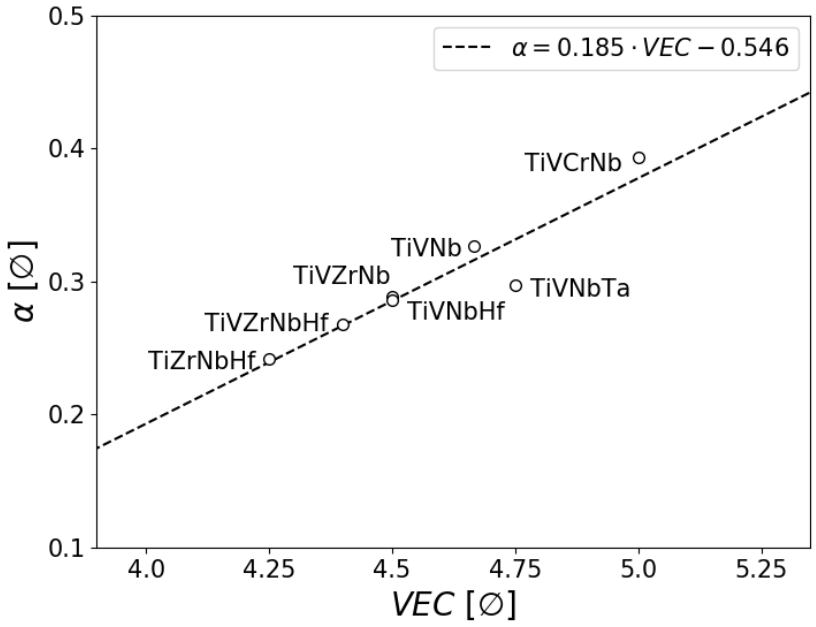

Fig. 3: Correlation between the valence-electron concentration *VEC* and the expansion of the volume per metal atom from the bcc HEA to the corresponding hydride α that is defined in equation 2 for the considered HEAs. The error bars are within the data points.

where $(V/Z)_{\mathrm{bcc}}$ and $(V/Z)_{\mathrm{fcc}}$ are the volumes per metal atom in the bcc and fcc lattices, respectively. Fig. 3 shows that α increases linearly with the *VEC* following the relation

$$\alpha = 0.185 \cdot VEC - 0.546 \tag{3}$$

The smallest and largest expansion in the volume per metal atom observed in this study is 24% and 39% for the TiZrNbHf and TiVCrNb systems, respectively.

Fig. 4 presents the manometric and gravimetric measurements for the hydrogen contents of the synthesized hydrides. The manometric measurements

show [H]/[M] close to 2 for the lowest *VEC*. If $VEC \geq 5.0$ the manometric measurements indicate lower hydrogen content. For example, the highest observed hydrogen content for TiVCrMo ($VEC = 5.25$) is [H]/[M] = 0.75, and in this case a fcc hydride is not achieved with pressures as high as 100 bar H_2. It is likely that this marks the transition between the first and second plateau in the pressure-composition isotherm, and that the plateau pressure is higher than the H_2 pressures applied in this study. Fig. 4 shows that the manometric and gravimetric measurements agree when $VEC < 4.75$. Beyond this limit the manometric measurements are larger than the gravimetric ones, and thus indicating outgassing of hydrogen when the material is removed from the autoclave. The TG/DSC measurements conducted during desorption of hydrogen from a representative selection of the hydrides are presented in fig. 5. The corresponding measurements for the other hydrides are shown in fig. A.4 in the supplementary information. For the most stable hydrides, the desorptions consist of two events. If $TiVCrNbH_x$ is left in the glovebox at *RT* and 1 bar Ar for 100 days, the hydride spontaneously desorbs H_2, and thus the structure changes from fcc to bcc. When TG/DSC is measured on the resultant hydride, the first desorption step is not observed while the second is still present. The first event is not observed for $TiVCrNbMoH_x$ and $TiVCrMoH_x$. In these cases a fcc hydride is never achieved in the first place. These observations suggests that the first event corresponds to the transition from a fcc dihydride to a bcc monohydride. The second event would then be the transition from a bcc monohydride to the hydrogen-free bcc alloy. Fig. 6 presents the onset temperature for the desorption for both events. The onset temperature of the first event is constant at $T_{onset} = 280$ °C when

$VEC \leq 4.67$. Above this limit, the onset temperature decreases indicating destabilization of the hydrides. Therefore, we expect that the deviation between the manometric and gravimetric measurements of the hydrogen contents can be explained by outgassing of hydrogen during transport from the high-pressure environment inside the Sieverts apparatus to the TG/DSC. Fig. 6 also shows that the second event is destabilized when VEC increases. In this case, the onset temperature for desorption T_{onset} decreases linearly with the VEC following the relation

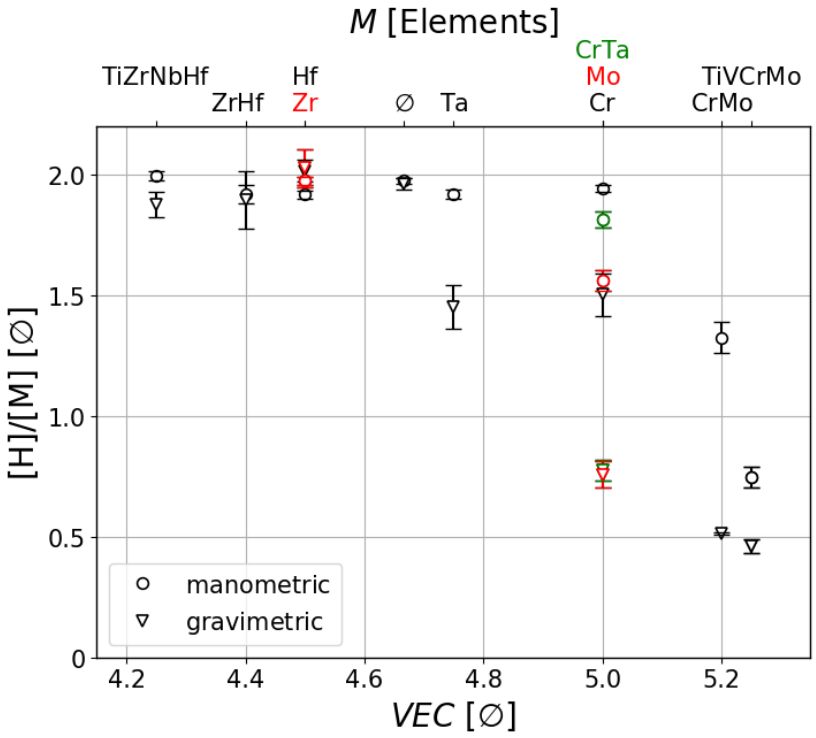

Fig. 4: The hydrogen-to-metal ratio [H]/[M] of the hydrides $TiVCrMoH_x$, $TiZrNbHfH_x$, $TiVNbMH_x$, $M \in \{\varnothing, Cr, Zr, Mo, Hf, Ta\}$, $TiVZrNbHfH_x$ ($M = ZrHf$), $TiVCrNbMoH_x$ ($M = CrMo$) and $TiVCrNbTaH_x$ ($M = CrTa$) determined by TGA in the TG/DSC apparatus and manometrically in the Sieverts apparatus.

$$T_{onset} = 1203\ ^{\circ}\mathrm{C} - (184\ ^{\circ}\mathrm{C}) \cdot VEC \tag{4}$$

Extrapolation suggests that $VEC = 6.00$ is needed to achieve desorption onset at 100 °C for the second event while $VEC = 6.40$ is needed to have onset at RT. It should be noted that the desorption appears to be slightly more complicated for TiZrNbHf, TiVZrNbHf and TiVZrNb because of additional endothermic events in the DSC signals between 400 and 800 °C. As these systems were observed to phase-separate during the desorption, we believe that the additional events are associated with desorption of hydrogen from the decomposition products. It should also be noted that an exothermic event with onset at $T = 746$ °C is observed for TiVCrNb. This is most likely where the compound phase-separates from the bcc HEA into the multiphase composition shown in fig. 2.

$TiVNbH_x$ and the two most unstable hydrides for which dihydrides were obtained, $TiVNbTaH_x$ and $TiVCrNbH_x$, were cycled between 23 ± 2 bar H_2 and dynamic vacuum at RT. Fig. 7 shows that $TiVNbH_x$ has very little reversible hydrogen storage capacity under these conditions. On the contrary, $TiVNbTaH_x$ has a reversible capacity of 0.92 wt.% H ([H]/[M] = 0.85) after one absorption/desorption cycle. The reversible capacity is unfortunately reduced to zero after five absorption/desorption cycles. TG/DSC confirms that the reduction in reversible capacity corresponds to a capacity-loss as the remaining hydrogen content in the sample is 1.24 wt.% H ([H]/[M] = 1.15). This is lower than what was observed for the same system after only one cycle (see fig. 4). PXD reveal that the reduction in reversible capacity is accompanied by structural changes when compared to the as cast alloy. After one

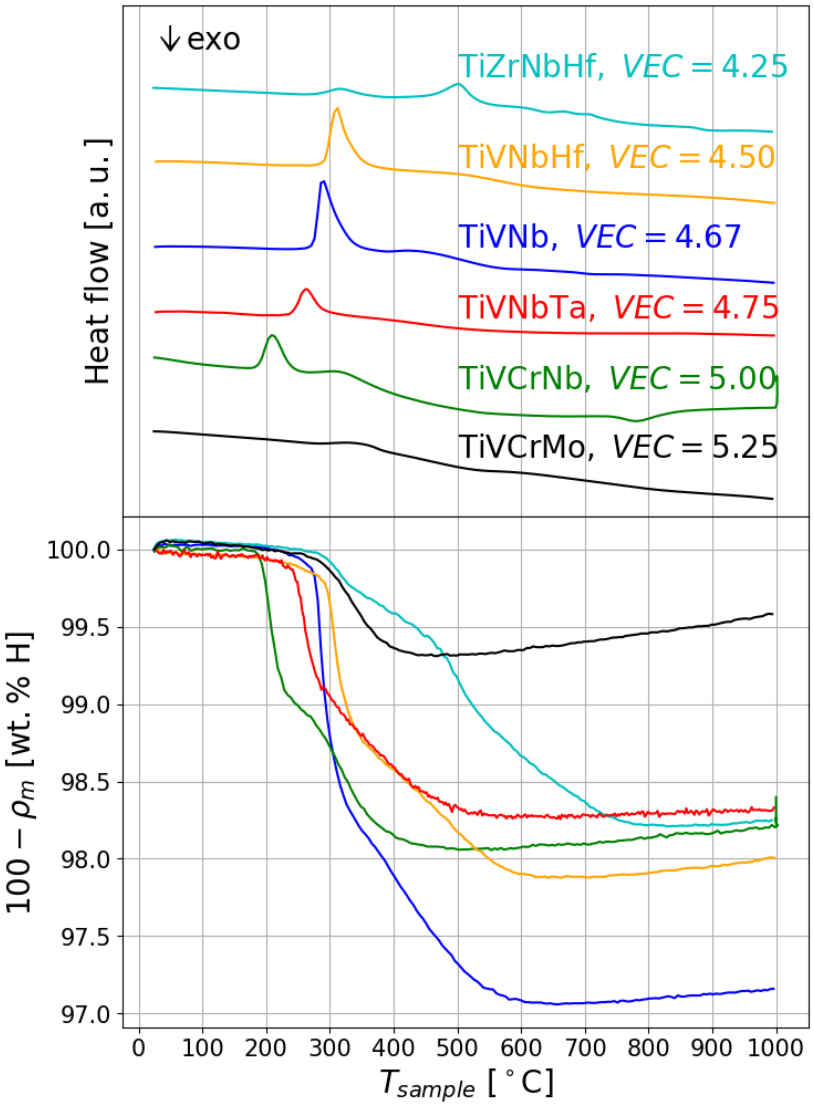

Fig. 5: TG/DSC measurements during hydrogen desorption from TiVNbMH$_x$, $M \in \{\varnothing, \mathrm{Cr}, \mathrm{Hf}, \mathrm{Ta}\}$, TiZrNbHfH$_x$ and TiVCrMoH$_x$ at a constant heating-rate of 10 °C/min. The upper part of the figure show the DSC heat flow signals while the corresponding mass loss ρ_m that is assumed to be solely due to desorption of hydrogen is shown in the lower part.

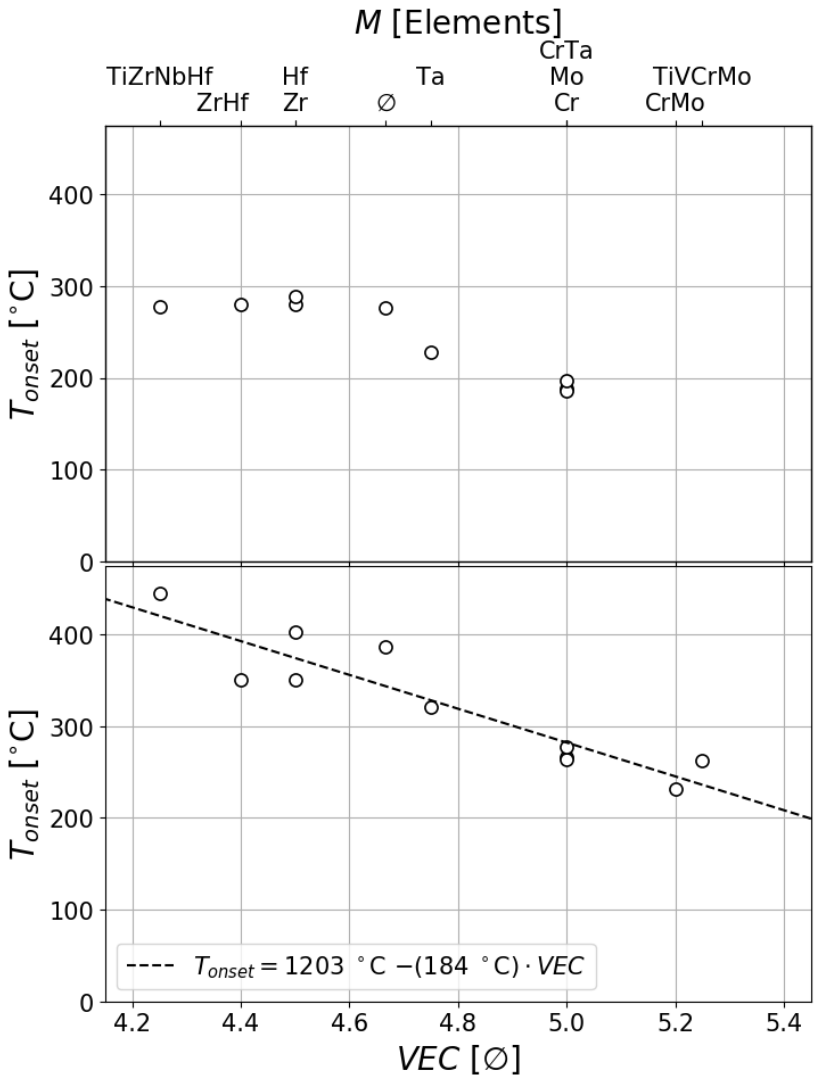

Fig. 6: The onset temperatures T_{onset} for desorption of hydrogen from the investigated HEA-based hydrides as a function of the valence-electron concentration *VEC*. The onset temperature for the first and second event is shown in the upper and lower panel, respectively. Notice that there is a linear correlation between the onset temperature of the second event and *VEC*.

absorption/desorption cycle, a new peak has appeared on the low-angle side of the 110 reflection of the main phase. At this point, no other new peaks can be resolved. After ten absorption/desorption cycles, more peaks can be resolved and it is evident that a bcc impurity phase with lattice parameter $a_{\mathrm{bcc}} = 3.3000(4)$ Å has formed. This is very similar to the lattice parameter of bcc-Ta [39] and suggests that Ta separates out of the HEA during cycling. This also seems reasonable from a SEM perspective as obvious Ta-rich and Ta-poor areas can be observed in this alloy [34]. In the case of $\mathrm{TiVCrNbH_8}$, a reversible hydrogen storage capacity of 1.96 wt.% H is observed. This is significantly higher than $\mathrm{LaNi_5H_6}$, and comparable to $\mathrm{TiFeH_2}$. It is also interesting that the volumetric hydrogen storage capacity of this material is 158 g/L which is higher than the current record of 150 g/L ($\mathrm{Mg_2FeH_6}$) in transition metal hydrides [15]. Furthermore, the absorption kinetics are very fast, and the reaction is for all practical purposes complete within few minutes. However, the desorption commenced slowly and a complete desorption could only be obtained if the system was placed under dynamic vacuum for at least five hours. No structural changes could be observed by PXD after ten absorption/desorption cycles.

A series of Kissinger analyses were performed on the DSC heat flow signals measured on the systems $\mathrm{TiVNb}M\mathrm{H_x}$, $M \in \{\varnothing, \mathrm{Cr}, \mathrm{Zr}, \mathrm{Mo}, \mathrm{Hf}, \mathrm{Ta}\}$ and $\mathrm{TiVZrNbHfH_x}$ to investigate the desorption kinetics further. The Kissinger analyses of the endothermal desorption events are shown in fig. 8. The activation energy of the first event is significantly higher for $\mathrm{TiVNbH_x}$ as compared to the other hydrides. Therefore, it seems that the desorption kinetics is enhanced if an additional element is added to the HEA. Among the

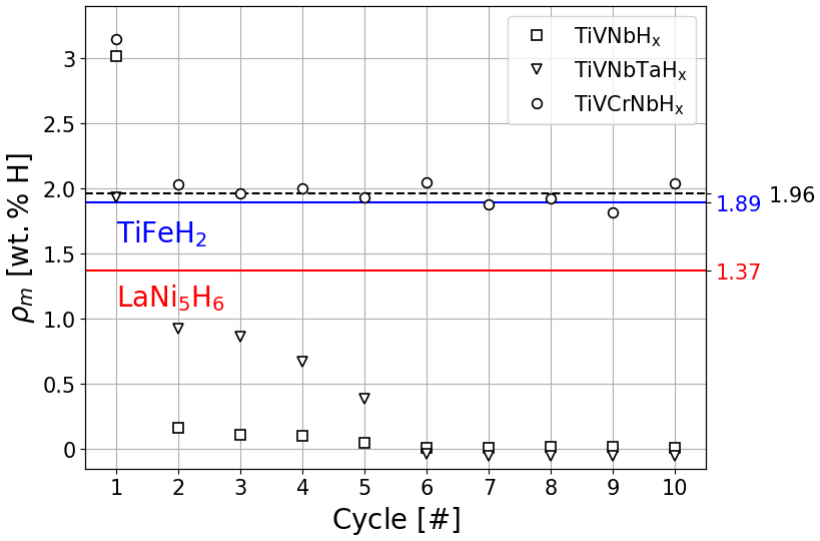

Fig. 7: The reversible hydrogen storage capacity ρ_m measured during absorption/desorption cycles between dynamic vacuum and 23 ± 2 bar H_2 at room-temperature for $TiVNbH_x$, $TiVNbTaH_x$ and $TiVCrNbH_x$. The black dashed line indicate the mean value of the reversible hydrogen storage capacity in $TiVCrNbH_x$. As a reference, the reversible hydrogen storage capacity of $LaNi_5H_6$ and $TiFeH_2$ are indicated by the red and blue solid lines, respectively. The error bars are within the data points.

quaternary HEA-based hydrides there are no significant differences in the activation energies. This indicates that the desorption kinetics are comparable for these systems. If yet another element is added, as in $TiVZrNbHfH_x$, the desorption kinetics are not enhanced further. The activation energy of the second event is similar for all the investigated hydrides. As there are no systematic variation in the activation energies with respect to the VEC, the destabilization process can not be explained by enhanced desorption kinetics alone. Thus, it seems that the destabilization process is a thermodynamic effect.

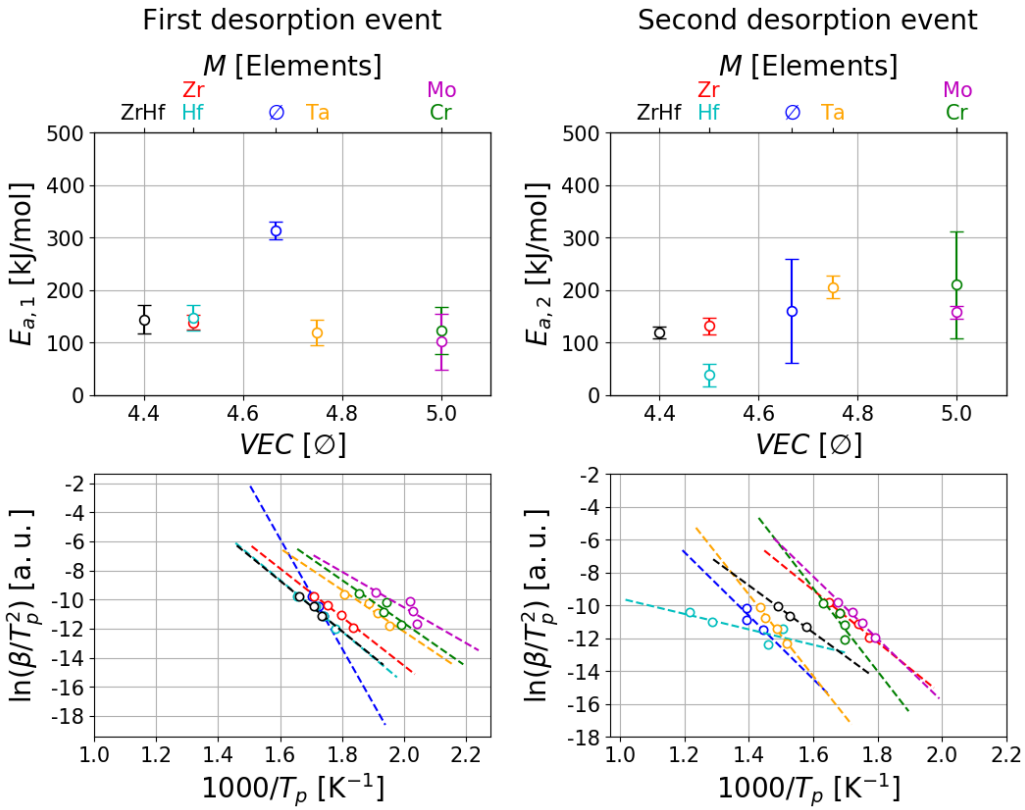

Fig. 8: Activation energies $E_{a,\cdot}$ for the two different events determined by Kissingers method performed on DSC measurements during desorption of hydrogen from TiVNbMH$_x$, $M = \varnothing, \mathrm{Cr}, \mathrm{Zr}, \mathrm{Mo}, \mathrm{Hf}, \mathrm{Ta}$ and TiVZrNbHfH$_x$. The figures in the upper row show the activation energies $E_{a,\cdot}$ as a function of the valence-electron concentration VEC while the figures in the lower row show the corresponding Kissinger analyses.

4. Conclusions

The present systematic investigation of the structure and hydrogen storage properties of a series of quaternary and quintary high-entropy alloys (HEAs) has revealed a series of interesting trends. All the considered alloys assume body-centred cubic (bcc) crystal structures and form face-centred

cubic (fcc) hydrides if the valence-electron concentration $VEC \leq 5.00$. The volume expansion per metal atom increase linearly with the VEC of the HEA from the bcc alloy to the corresponding hydride. The hydrogen desorption occurs in two steps. First, the fcc dihydride decomposes into a bcc monohydride. Then, the bcc monohydride decomposes into the hydrogen-free alloy. When the $VEC > 4.75$, the dihydride is destabilized and the hydride spontaneously desorbs hydrogen when it is removed from the high hydrogen pressures after synthesis. A linear correlation is observed between the onset temperature for the desorption of hydrogen from the bcc monohydride to the hydrogen-free alloy. When $VEC \geq 5$, the maximum hydrogen storage capacity is reduced, meaning that [H]/[M] < 2.0. Thus, it seems that a larger VEC destabilizes the hydrides, and eventually the destabilization results in a reduction in the maximal hydrogen storage capacity.

Based on these insights we have identified $TiVCrNbH_8$ ($VEC = 5.0$) as a promising hydrogen storage material. This HEA-based hydride exhibits a reversible hydrogen storage capacity of 1.96 wt.% H at RT and moderate pressures. Moreover, it is not dependent on elaborate activation procedures to absorb hydrogen. Hence, $TiVCrNbH_8$ prevail at many of the classical show-stoppers for hydrogen storage in transition-metal-based hydrides. We acknowledge that the proposed alloy still suffers from being based on expensive elements, such as V and Nb. Nevertheless, the insights provided might serve as a road-map towards developing novel bcc HEA-based metal hydrides that are cost-efficient and reversible at RT with higher gravimetric hydrogen capacities.

Acknowledgements

This work is funded by the NordForsk Nordic Neutron Science Programme through the functional hydrides (FunHy) project (grant number 81942). The skilful assistance of the staff at the Swiss-Norwegian beamline at the European Synchrotron Radiation Facility in Grenoble, France is greatly acknowledged. Dennis Karlsson acknowledge support from the Swedish Foundation for Strategic Research through the SSF - Development of processes and Materials in the AM project (reference number GMT14-0048).

Appendix A. Supplementary data

Supplementary data to this article can be found online at ... .

References

[1] J. Conti, P. Holtberg, J. Diefenderfer, A. LaRose, J. T. Turnure, L. Westfall, International energy outlook 2016 with projections to 2040, Technical Report, USDOE Energy Information Administration (EIA), Washington, DC (United States). Office of Energy Analysis, 2016.

[2] M. V. Lototskyy, I. Tolj, L. Pickering, C. Sita, F. Barbir, V. Yartys, The use of metal hydrides in fuel cell applications, Progress in Natural Science: Materials International 27 (2017) 3–20.

[3] J. B. von Colbe, J.-R. Ares, J. Barale, M. Baricco, C. Buckley, G. Capurso, N. Gallandat, D. M. Grant, M. N. Guzik, I. Jacob, et al., Application of hydrides in hydrogen storage and compression: Achievements,

outlook and perspectives, International Journal of Hydrogen Energy 44 (2019) 7780–7808.

[4] J. Graetz, Y. Lee, J. Reilly, S. Park, T. Vogt, Structures and thermodynamics of the mixed alkali alanates, Physical Review B 71 (2005) 184115.

[5] B. Bogdanović, R. A. Brand, A. Marjanović, M. Schwickardi, J. Tölle, Metal-doped sodium aluminium hydrides as potential new hydrogen storage materials, Journal of Alloys and Compounds 302 (2000) 36–58.

[6] S.-i. Orimo, Y. Nakamori, J. R. Eliseo, A. Züttel, C. M. Jensen, Complex hydrides for hydrogen storage, Chemical Reviews 107 (2007) 4111–4132.

[7] M. Paskevicius, L. H. Jepsen, P. Schouwink, R. Černỳ, D. B. Ravnsbæk, Y. Filinchuk, M. Dornheim, F. Besenbacher, T. R. Jensen, Metal borohydrides and derivatives–synthesis, structure and properties, Chemical Society Reviews 46 (2017) 1565–1634.

[8] C. Frommen, M. Sørby, M. Heere, T. Humphries, J. Olsen, B. Hauback, Rare earth borohydrides-crystal structures and thermal properties, Energies 10 (2017) 2115.

[9] C. Milanese, T. Jensen, B. Hauback, C. Pistidda, M. Dornheim, H. Yang, L. Lombardo, A. Zuettel, Y. Filinchuk, P. Ngene, et al., Complex hydrides for energy storage, International Journal of Hydrogen Energy 44 (2019) 7860–7874.

[10] R. Cohen, K. West, J. Wernick, Degradation of LaNi5 by temperature-induced cycling, Journal of the Less Common Metals 73 (1980) 273–279.

[11] L. Schlapbach, T. Riesterer, The activation of FeTi for hydrogen absorption, Applied Physics A 32 (1983) 169–182.

[12] J. Joubert, M. Latroche, A. Percheron-Guégan, Hydrogen absorption properties of several intermetallic compounds of the ZrNi system, Journal of Alloys and Compounds 231 (1995) 494–497.

[13] N. Rusman, M. Dahari, A review on the current progress of metal hydrides material for solid-state hydrogen storage applications, International Journal of Hydrogen Energy 41 (2016) 12108–12126.

[14] G. Walker, Solid-state hydrogen storage: materials and chemistry, Elsevier, 2008.

[15] J. Huot, D. B. Ravnsbæk, J. Zhang, F. Cuevas, M. Latroche, T. R. Jensen, Mechanochemical synthesis of hydrogen storage materials, Progress in Materials Science 58 (2013) 30–75.

[16] H. Chung, J.-Y. Lee, Effect of partial substitution of Mn and Ni for Fe in FeTi on hydriding kinetics, International Journal of Hydrogen Energy 11 (1986) 335–339.

[17] S. W. Lambert, D. Chandra, W. N. Cathey, F. E. Lynch, R. C. Bowman Jr, Investigation of hydriding properties of LaNi4.8Sn0.2, LaNi4.27Sn0.24 and La0.9Gd0.1Ni5 after thermal cycling and aging, Journal of Alloys and Compounds 187 (1992) 113–135.

[18] B.-H. Liu, D.-M. Kim, K.-Y. Lee, J.-Y. Lee, Hydrogen storage properties of TiMn2-based alloys, Journal of Alloys and Compounds 240 (1996) 214–218.

[19] D. Miracle, O. Senkov, A critical review of high entropy alloys and related concepts, Acta Materialia 122 (2017) 448–511.

[20] S. Guo, C. Ng, J. Lu, C. Liu, Effect of valence electron concentration on stability of fcc or bcc phase in high entropy alloys, Journal of Applied Physics 109 (2011) 103505.

[21] M. Poletti, L. Battezzati, Electronic and thermodynamic criteria for the occurrence of high entropy alloys in metallic systems, Acta Materialia 75 (2014) 297–306.

[22] Y.-F. Kao, S.-K. Chen, J.-H. Sheu, J.-T. Lin, W.-E. Lin, J.-W. Yeh, S.-J. Lin, T.-H. Liou, C.-W. Wang, Hydrogen storage properties of multi-principal-component CoFeMnTixVyZrz alloys, International Journal of Hydrogen Energy 35 (2010) 9046–9059.

[23] I. Kunce, M. Polanski, J. Bystrzycki, Structure and hydrogen storage properties of a high entropy zrtivcrfeni alloy synthesized using laser engineered net shaping (LENS), International Journal of Hydrogen Energy 38 (2013) 12180–12189.

[24] I. Kunce, M. Polanski, J. Bystrzycki, Microstructure and hydrogen storage properties of a TiZrNbMoV high entropy alloy synthesized using laser engineered net shaping (LENS), International Journal of Hydrogen Energy 39 (2014) 9904–9910.

[25] M. Sahlberg, D. Karlsson, C. Zlotea, U. Jansson, Superior hydrogen storage in high entropy alloys, Scientific Reports 6 (2016).

[26] I. Kunce, M. Polański, Czujko, Microstructures and hydrogen storage properties of LaNiFeVMn alloys, International Journal of Hydrogen Energy 42 (2017) 27154–27164.

[27] D. Karlsson, G. Ek, J. Cedervall, C. Zlotea, K. T. Møller, T. C. Hansen, J. Bednarcik, M. Paskevicius, M. H. Sørby, T. R. Jensen, U. Jansson, M. Sahlberg, Structure and hydrogenation properties of a HfNbTiVZr high-entropy alloy, Inorganic Chemistry 57 (2018) 2103–2110.

[28] S.-K. Chen, P.-H. Lee, H. Lee, H.-T. Su, Hydrogen storage of C14-CruFevMnwTixVyZrz alloys, Materials Chemistry and Physics 210 (2018) 336–347.

[29] G. Zepon, D. Leiva, R. Strozi, A. Bedoch, S. Figueroa, T. Ishikawa, W. Botta, Hydrogen-induced phase transition of MgZr-TiFe0.5Co0.5Ni0.5 high entropy alloy, International Journal of Hydrogen Energy 43 (2018) 1702–1708.

[30] C. Zlotea, M. Sow, G. Ek, J.-P. Couzinié, L. Perrière, I. Guillot, J. Bourgon, K. Møller, T. Jensen, E. Akiba, M. Sahlberg, Hydrogen sorption in TiZrNbHfTa high entropy alloy, Journal of Alloys and Compounds 775 (2018) 667–674.

[31] C. Zhang, Y. Wu, L. You, X. Cao, Z. Lu, X. Song, Investigation on the activation mechanism of hydrogen absorption in TiZrNbTa high entropy alloy, Journal of Alloys and Compounds 781 (2019) 613–620.

[32] H. Shen, J. Zhang, J. Hu, J. Zhang, Y. Mao, H. Xiao, X. Zhou, X. Zu, A novel TiZrHfMoNb high-entropy alloy for solar thermal energy storage, Nanomaterials 9 (2019) 248.

[33] J. Hu, H. Shen, M. Jiang, H. Gong, H. Xiao, Z. Liu, G. Sun, X. Zu, A DFT study of hydrogen storage in high-entropy alloy TiZrHfScMo, Nanomaterials 9 (2019) 461.

[34] M. M. Nygård, G. Ek, D. Karlsson, M. Sahlberg, M. H. Sørby, B. C. Hauback, Hydrogen storage in high-entropy alloys with varying degree of local lattice strain, International Journal of Hydrogen Energy (2019). DOI: https://doi.org/10.1016/j.ijhydene.2019.03.223.

[35] H. Brinks, A. Fossdal, R. Bowman, B. Hauback, Pressure–composition isotherms of TbNiAlHx, Journal of Alloys and Compounds 417 (2006) 92–95.

[36] V. Dyadkin, P. Pattison, V. Dmitriev, D. Chernyshov, A new multipurpose diffractometer PILATUS @ SNBL, Journal of Synchrotron Radiation 23 (2016).

[37] B. H. Toby, R. B. Von Dreele, GSAS-II: the genesis of a modern open-source all purpose crystallography software package, Journal of Applied Crystallography 46 (2013) 544–549.

[38] P. Thompson, D. Cox, J. Hastings, Rietveld refinement of Debye–Scherrer synchrotron X-ray data from Al2O3, Journal of Applied Crystallography 20 (1987) 79–83.

[39] G. Brauer, K. H. Zapp, Die nitride des tantals, Zeitschrift für anorganische und allgemeine Chemie 277 (1954) 129–139.